



**CHALMERS**  
UNIVERSITY OF TECHNOLOGY

## **A Novel Aqueous Asymmetric Supercapacitor based on Pyrene-4,5,9,10-Tetraone Functionalized Graphene as the Cathode and**

Downloaded from: <https://research.chalmers.se>, 2024-04-09 20:35 UTC

Citation for the original published paper (version of record):

Shi, M., Peng, C., Zhang, X. (2023). A Novel Aqueous Asymmetric Supercapacitor based on Pyrene-4,5,9,10-Tetraone Functionalized Graphene as the Cathode and Annealed Ti<sub>3</sub>C<sub>2</sub>Tx MXene as the Anode. *Small*, 19: 2301449-. <http://dx.doi.org/10.1002/sml.202301449>

N.B. When citing this work, cite the original published paper.

# A Novel Aqueous Asymmetric Supercapacitor based on Pyrene-4,5,9,10-Tetraone Functionalized Graphene as the Cathode and Annealed $\text{Ti}_3\text{C}_2\text{T}_x$ MXene as the Anode

Mangmang Shi, Cheng Peng, and Xiaoyan Zhang\*

Asymmetric supercapacitors (ASCs), employing two dissimilar electrode materials with a large redox peak position difference as cathode and anode, have been designed to further broaden the voltage window and improve the energy density of supercapacitors. Organic molecule based electrodes can be constructed by combining redox-active organic molecules with conductive carbon-based materials such as graphene. Herein, pyrene-4,5,9,10-tetraone (PYT), a redox-active molecule with four carbonyl groups, exhibits a four-electron transfer process and can potentially deliver a high capacity. PYT is noncovalently combined with two different kinds of graphene (Graphenea [GN] and LayerOne [LO]) at different mass ratios. The PYT-functionalized GN electrode (PYT/GN 4–5) possesses a high capacity of  $711 \text{ F g}^{-1}$  at  $1 \text{ A g}^{-1}$  in  $1 \text{ M H}_2\text{SO}_4$ . To match with the PYT/GN 4–5 cathode, an annealed- $\text{Ti}_3\text{C}_2\text{T}_x$  (A- $\text{Ti}_3\text{C}_2\text{T}_x$ ) MXene anode with a pseudocapacitive character is prepared by pyrolysis of pure  $\text{Ti}_3\text{C}_2\text{T}_x$ . The assembled PYT/GN 4–5//A- $\text{Ti}_3\text{C}_2\text{T}_x$  ASC delivers an outstanding energy density of  $18.4 \text{ Wh kg}^{-1}$  at a power density of  $700 \text{ W kg}^{-1}$ . The PYT-functionalized graphene holds great potential for high-performance energy storage devices.

(> $10^5$  cycles).<sup>[4–6]</sup> However, the working voltage window of aqueous electrolyte energy storage systems is always narrow due to the limitation of water thermodynamic decomposition voltage ( $\approx 1.23 \text{ V}$ ).<sup>[7]</sup> Furthermore, the low operation voltage results in inferior energy density, because the energy density ( $E$ ) is mainly determined by the working voltage ( $V$ ) and the specific capacitance of electrode ( $C$ ) according to the formula  $E = 1/2 CV^2$ .<sup>[8–10]</sup> Fortunately, the fabrication of aqueous asymmetric supercapacitors (ASCs), employing two dissimilar electrode materials with a large redox peak position difference as cathode and anode, can effectively suppress the thermodynamic limitation of water molecules<sup>[11]</sup> and take the advantages of well-matched paired electrodes working potential to widen the operating voltage window, providing an opportunity to improve the energy density.<sup>[12]</sup> Therefore, the search for cost-effective,

high capacity of advanced cathode and anode materials for ASCs has garnered the spotlight of worldwide research.

Currently, carbon-based electrode materials (e.g., graphene, carbon nanotubes, carbon quantum dots, etc.), as typical capacitive-type electrodes, have dominated the commercial SCs market.<sup>[13–17]</sup> Despite the satisfactory power density originating from the typical physical adsorption/desorption of ions, carbonaceous materials are still suffering from insufficient energy density ( $<10 \text{ Wh kg}^{-1}$ ) due to the lack of electroactive groups.<sup>[18]</sup> By contrast, pseudocapacitive materials such as metal oxides (e.g.,  $\text{RuO}_2$ ,<sup>[19,20]</sup>  $\text{MnO}_2$ ,<sup>[21]</sup>  $\text{MoO}_3$ ,<sup>[22]</sup> etc.<sup>[23]</sup>), conductive polymers (e.g., polyaniline<sup>[24]</sup> and polythiophene<sup>[25]</sup>) and small organic molecules (e.g., hydroquinone,<sup>[26]</sup> p-phenylenediamine,<sup>[27]</sup> and 3,4,5-trihydroxybenzamide<sup>[28]</sup>), can undergo fast faradaic redox reactions occurring at or near the surface of electrodes, holding great potential for serving as advanced cathode materials in energy storage devices with high energy density and high power density simultaneously.<sup>[29,30]</sup> Among all the available pseudocapacitive materials, redox-active carbonyl-containing organic molecules (e.g., quinone, ketone, and carboxylate) have attracted much attention in ASCs for the features of relatively low-cost, chemical and structural diversity, rich oxidation/reduction conversion sites, and fast reaction kinetics.<sup>[31]</sup> However, the practical application of these organic molecules in ASCs is still hindered by

## 1. Introduction

Design and fabrication of efficient, low-cost, and sustainable electrochemical energy storage devices are of grand importance to meet the future demand for greener energy to mitigate global warming.<sup>[1–3]</sup> Among them, aqueous supercapacitors (SCs) have received tremendous attention, especially in grid-scale applications, due to the merits of low cost, environmental benignity, nonflammability, high power density, and ultralong lifespan

M. Shi, C. Peng, X. Zhang  
Department of Chemistry and Chemical Engineering  
Chalmers University of Technology  
Kemigården 4, Göteborg SE-412 96, Sweden  
E-mail: xiaoyan.zhang@chalmers.se

M. Shi  
School of physics  
Xi'an Jiaotong University  
Xi'an 710049, P. R. China

The ORCID identification number(s) for the author(s) of this article can be found under <https://doi.org/10.1002/smll.202301449>.

© 2023 The Authors. Small published by Wiley-VCH GmbH. This is an open access article under the terms of the Creative Commons Attribution License, which permits use, distribution and reproduction in any medium, provided the original work is properly cited.

DOI: 10.1002/smll.202301449

the low electrical conductivity and the inevitable dissolution in the electrolyte during charge-discharge processes. To solve the aforementioned issues, grafting organic molecules on the surface of carbon substrates via covalent or noncovalent strategies has been proven to be promising and effective.<sup>[32]</sup> Compared with covalent approaches, noncovalent interactions (e.g.,  $\pi$ - $\pi$  stacking) do not largely interrupt the  $\pi$ -conjugated system of the carbon backbone while insuring its high electrical conductivity and structural stability.<sup>[33,34]</sup> Notably, compared with other carbon materials, graphene and its derivatives are widely investigated for its high conductivity, large surface area, superior capacitive performance, and ease of functionalization.<sup>[35–42]</sup> In addition, as a typical carbonyl-containing organic molecule, pyrene-4,5,9,10-tetraone (PYT) possesses four carbonyl functional groups and shows a symmetrical conjugated structure, which can contribute to an excellent specific capacity and can guarantee the electrochemical stability during redox processes.<sup>[43]</sup> Therefore, rational design and construction of PYT-functionalized graphene cathode are expected to take advantage of both the PYT molecules and graphene, resulting in an enhancement of the electrochemical performance.

In order to match with the PYT-functionalized graphene cathode, titanium carbide ( $\text{Ti}_3\text{C}_2\text{T}_x$ ) MXene was selected as the anode, which can be attributed to the easy oxidation characteristic at anodic oxidation potentials.<sup>[44–46]</sup> Moreover,  $\text{Ti}_3\text{C}_2\text{T}_x$  MXene offers tremendous competitiveness to serve as active materials for supercapacitors, in terms of a) metallic-like conductivity, b) 2D lamellar structure, and c) a high capacitance under negative potentials based on pseudocapacitance mechanism.<sup>[47–50]</sup> Hence, the fabrication of all-pseudocapacitive ASCs, employing PYT-functionalized graphene as the cathode and  $\text{Ti}_3\text{C}_2\text{T}_x$  MXene as the anode, provides an inspiration for the next-generation energy storage devices with high energy and power density.

In the present approach, the PYT molecules were combined with two different kinds of graphene (GN and LO) via non-covalent interactions. The PYT-functionalized graphene shows excellent electrochemical performance due to  $\pi$ - $\pi$  interactions between the two species, which can facilitate the charge transfer between the PYT molecules and the graphene nanosheets. As a result, the PYT/GN 4–5 electrode shows a high specific capacity of  $711 \text{ F g}^{-1}$  at  $1 \text{ A g}^{-1}$  in  $1 \text{ M H}_2\text{SO}_4$ . Additionally, the A- $\text{Ti}_3\text{C}_2\text{T}_x$  anode shows a higher specific capacity of  $431 \text{ F g}^{-1}$  at  $3 \text{ A g}^{-1}$  than that of the pure  $\text{Ti}_3\text{C}_2\text{T}_x$  MXene anode ( $310 \text{ F g}^{-1}$  at  $3 \text{ A g}^{-1}$ ). The assembled PYT/GN 4–5//A- $\text{Ti}_3\text{C}_2\text{T}_x$  ASC delivers an outstanding energy density of  $18.4 \text{ Wh kg}^{-1}$  at a power density of  $700 \text{ W kg}^{-1}$ .

## 2. Results and Discussion

### 2.1. Material Characterization of Composites

The surface morphology and microstructure of all the samples were characterized by SEM. The as-prepared PYT molecules show a nanorod structure and the  $^1\text{H-NMR}$  spectrum further verifies the high purity of the PYT molecules (Figure S1, Supporting Information). As shown in Figure 1a, GN exhibits smooth, wavy, and pleated graphene sheets. With a large number of the PYT molecules being introduced (PYT/GN 8–1), ultrathin graphene nanosheets can be observed (Figure 1b), indicating that the presence of the PYT molecules does not destroy the structure of the graphene nanosheets. In addition, the PYT molecules, with a nanorod-like structure, stack on the surface of the GN (Figure 1b). As for the PYT/GN 4–5 electrode (Figure 1c), the graphene sheets still retain the structure. In contrast, the LO shows densely packed graphene sheets (Figure 1d) for its higher degree of reduction. As shown in Figure 1e,f, the PYT-functionalized LO electrodes (PYT/LO 4–5 and PYT/LO 2–7)

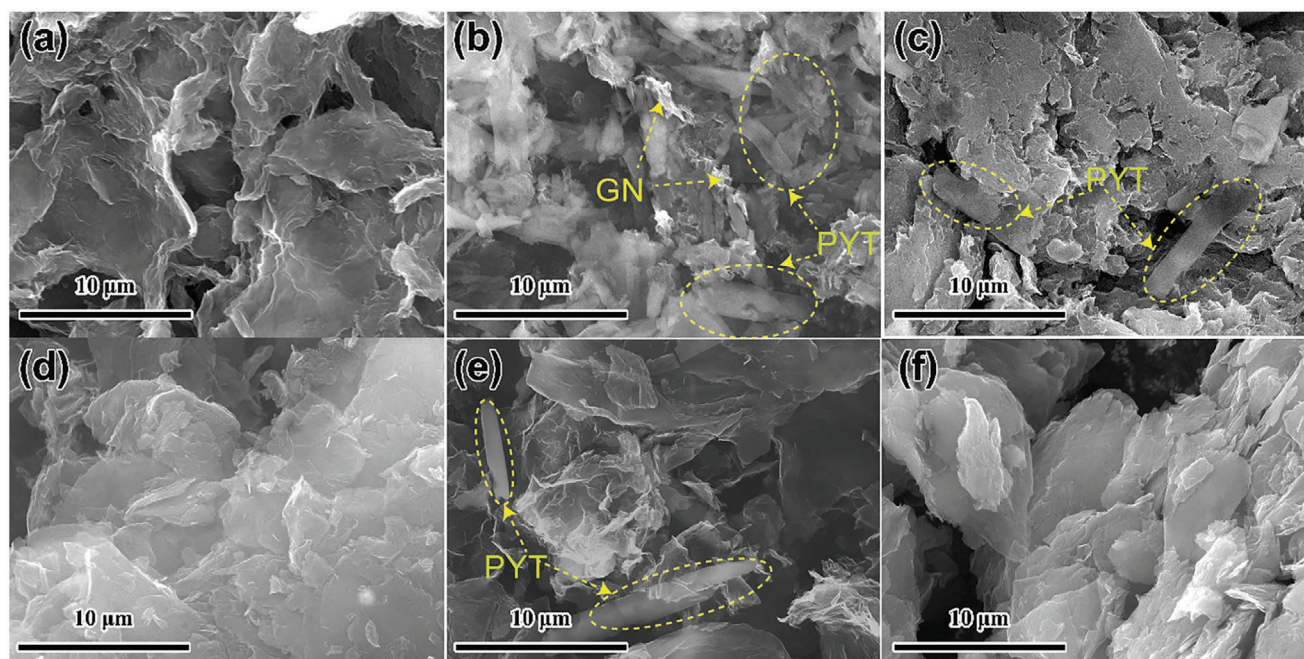


**Figure 1.** a–c) SEM images of GN, PYT/GN 8–1, and PYT/GN 4–5. d–f) SEM images of LO, PYT/LO 4–5 and PYT/LO 2–7.



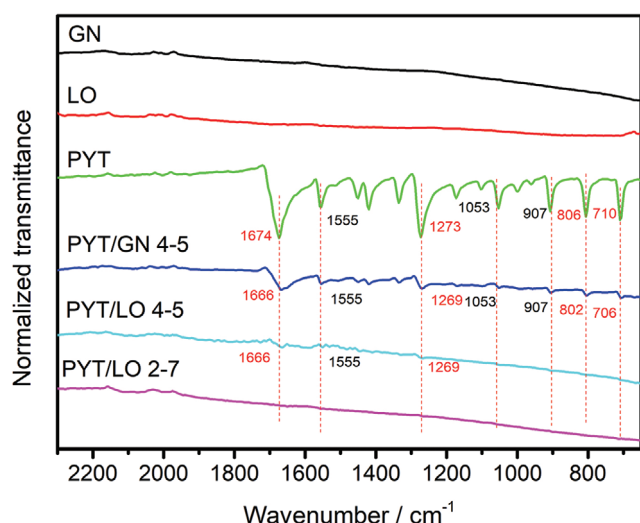


**Figure 2.** FT-IR spectra of GN, LO, PYT, PYT/GN 4–5, PYT/LO 4–5, and PYT/LO 2–7.

2–7) display a similar structure as the LO, with the PYT molecules clearly seen in the PYT/LO 4–5 sample (Figure 1e).

Fourier-transform infrared (FT-IR) spectroscopy (Figure 2) was performed to further characterize the interaction between the PYT molecules and the graphene nanosheets. It can be seen that the commercial graphene (GN and LO) has no pronounced absorption peaks, indicating that the oxygen-related groups have been largely removed from the surface of the graphene sheets. In addition, the pure PYT molecules show characteristic absorption peaks at  $\approx 1674$  and  $\approx 1273$   $\text{cm}^{-1}$ , which can be attributed to the stretching of the C=O group and the bending of the C–H bonds, respectively. Interestingly, compared with the PYT, the vibration of the C=O group and the C–H bonds in the PYT/GN 4–5 and the PYT/LO 4–5 composites shifts to a lower wavenumber, implying the existence of noncovalent  $\pi$ – $\pi$  interactions between the PYT molecules and the graphene nanosheets.<sup>[51,52]</sup> Besides, the intensity of the absorption peaks for the PYT/LO 4–5 is weaker than that of the PYT/GN 4–5 and even the

absorption peaks of the PYT/LO 2–7 composites disappeared, owing to the confinement effect of the PYT molecules within the LO, that is, the dipole changes of the functional groups on PYT are largely suppressed.

X-ray photoelectron spectroscopy (XPS) was used to study the chemical compositions of the pure PYT molecules, the two graphene samples, and their composites. As illustrated in Figure S2, Supporting Information, the wide-scan survey spectra of all the samples show a major C1s peak and a distinct O1s peak. Apparently, the PYT molecules possess an O content of 18.1%, deriving from the four carbonyl groups (Table S1, Supporting Information). After the combination with the PYT molecules, the O content reaches 15.2% for the PYT/GN 4–5 sample. In addition, the blank LO contains a low O content of 3.2% for its high degree of reduction, indicating a higher electrical conductivity (Table S3, Supporting Information). Due to the integration of the carbonyl groups, the PYT/LO 4–5 (6.4%) and the PYT/LO 2–7 (5.5%) composites demonstrate a larger O content. As shown in Figure 3a, the high-resolution C1s spectra of the PYT can be deconvoluted into two peaks located at the binding energies of 284.9 eV (C–C/C=C) and 287.4 eV (C=O), and the high-resolution C1s spectra of the GN and the PYT/GN 4–5 show two additional peaks of C–O (285.7 eV) and O–C=O (288.7 eV).<sup>[53,54]</sup> The corresponding O1s spectra of the PYT present only one peak at 531.9 eV, attributing to the C=O bond (Figure 3b). The O1s peak of the GN is deconvoluted into three significant peaks at 530.9, 532.05, and 533.5 eV, corresponding to the O–C=O, C=O, and C–O–C, respectively.<sup>[55]</sup> Compared with the pristine GN, the PYT/GN 4–5 demonstrates a higher percentage of the C=O bonds both in the C1s and the O1s spectra. Similarly, as displayed in Figure 3c and Figure 3d, the percentage of the C=O bonds of the electrodes for both the C1s and the O1s spectra follow the same trend: PYT/LO 4–5 > PYT/LO 2–7 > LO. The above XPS spectra results can prove that the PYT molecules have been successfully immobilized onto the graphene nanosheets. Moreover, compared with the pure LO sample and the LO-based composites, the pure GN sample and the GN-based composites show a higher surface area (Table S4, Supporting Information), which can provide more active sites

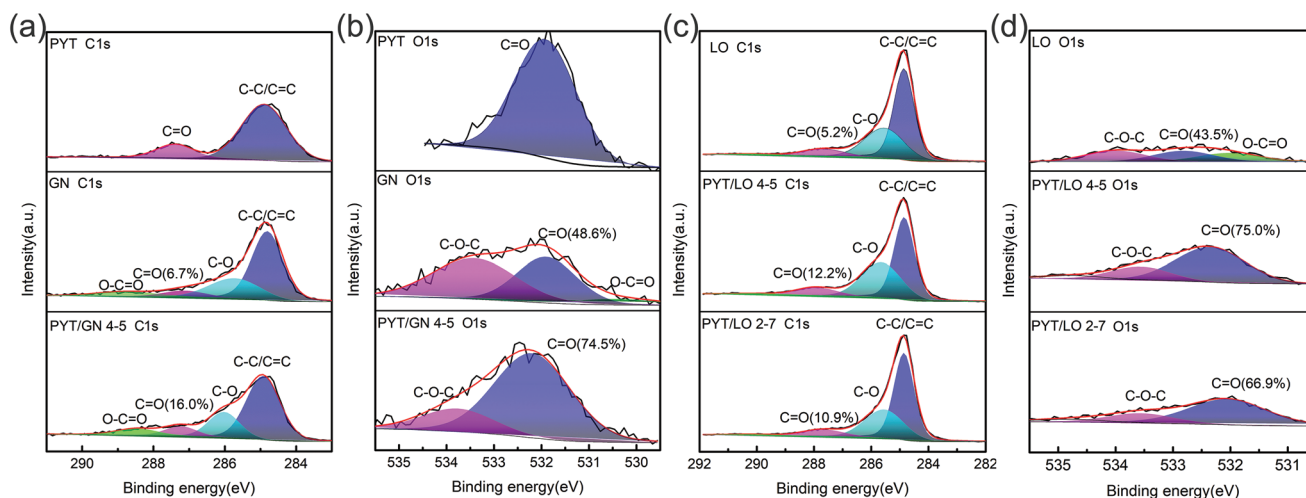


**Figure 3.** XPS deconvolution of C1s and O1s of a,b) PYT, GN, PYT/GN 4–5, and c,d) LO, PYT/LO 4–5, PYT/LO 2–7.

for the combination of the PYT molecules, shorten the ion diffusion path, and improve the electrochemical performance.

## 2.2. Electrochemical Measurement of Cathode

The electrochemical performance of the as-obtained GN and the PYT/GN electrodes at different ratios were assessed via cyclic voltammograms (CV) and galvanostatic charge-discharge (GCD) in a three-electrode setup in a 1 M H<sub>2</sub>SO<sub>4</sub> aqueous electrolyte. **Figure 4a** shows the comparison of all the CV curves at 10 mV s<sup>-1</sup>. Obviously, the GN exhibited a typical near-rectangle shape, suggesting that the electrical double-layer capacitive behavior dominates the charge storage process. After adding the PYT molecules, all the CV curves of the PYT/GN electrodes display two pairs of distinctly reversible redox peaks switching at  $\approx 0.23/0.17$  and  $\approx 0.37/0.30$  (vs Ag/AgCl), which can

be attributed to the redox reaction of the PYT (Figure S3, Supporting Information).<sup>[56]</sup> Moreover, the symmetric PYT molecule, with four carbonyl redox centers, exhibits a four-electron transfer process, implying that a higher output capacity can be gained.<sup>[31,57]</sup> Actually, the PYT/GN 8-1 electrode, with a low content of the conductive graphene, presents a relatively small CV integrated area, suggesting the inferior electrochemical activity and the low energy storage capacity due to the poor electrical conductivity of the PYT molecules (Table S3, Supporting Information). In addition, due to the lack of redox sites, the integrated area of the CV curve for the pure GN electrode is also small, which is approximately equal to that of the PYT/GN 8-1 electrode. After tuning the ratios between the PYT and the GN from 7-2 to 2-7, the PYT/GN 4-5 electrode with the optimized PYT:GN weight ratio of 4:5, shows the largest CV area, demonstrating its much larger capacitance and an excellent energy storage capacity. The corresponding GCD profiles of all the

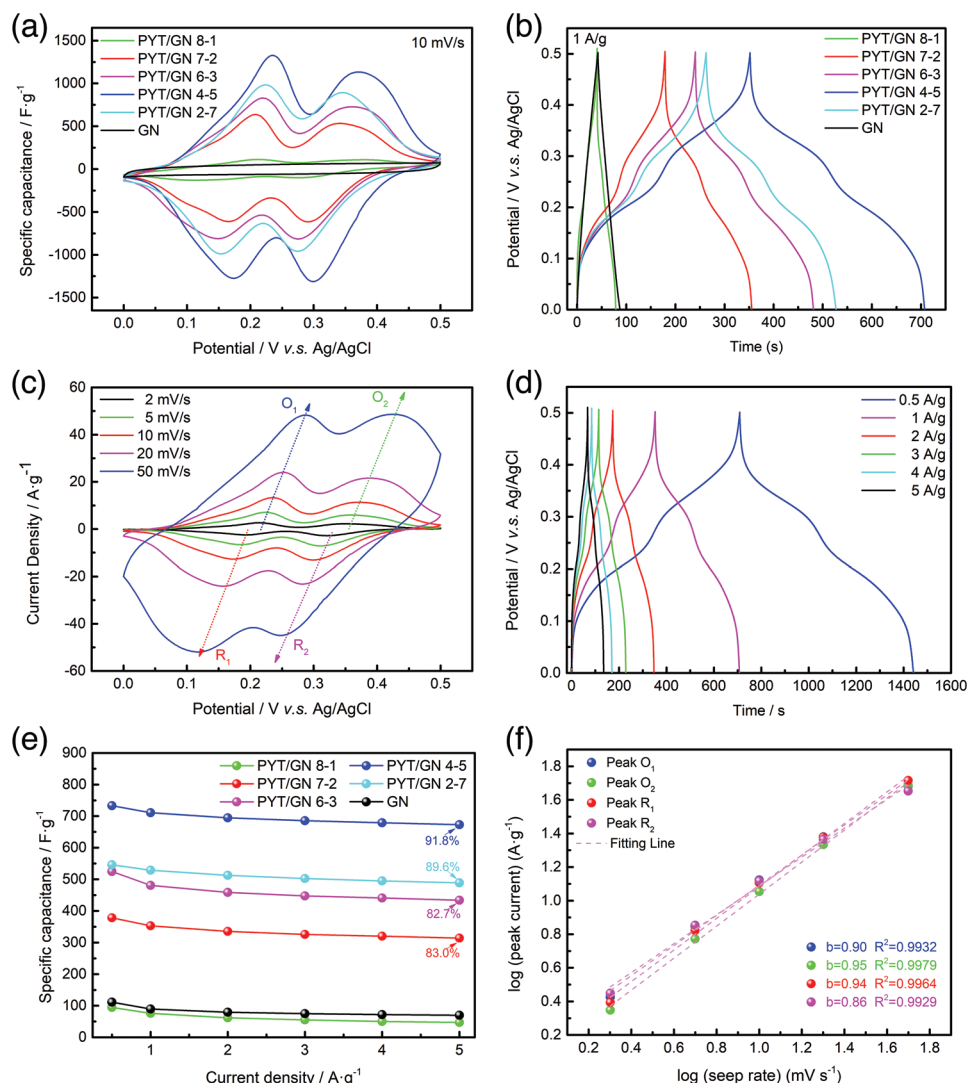


**Figure 4.** Electrochemical characterizations of different electrodes in a three-electrode system. a) CV curves at 10 mV s<sup>-1</sup> and b) GCD curves at 1 A g<sup>-1</sup>. c,d) CV curves at different scan rates and the corresponding GCD curves at various current densities of the PYT/GN 4-5 electrode. e) The specific capacity at various current densities and f) the relationship between peak current and scan rate.

electrodes at a current density of  $1 \text{ A g}^{-1}$  are shown in Figure 4b. Compared with the triangle-like shape of the GCD curves of the pure GN electrode, all the PYT/GN electrodes exhibit symmetrical and curved triangles, further reflecting the pseudocapacitive behavior of the composites.<sup>[58]</sup> In addition, the PYT/GN 4-5 electrode also shows a higher capacitance than other electrodes due to its much longer discharge time. The excellent electrochemical performance is caused by the reasonable component design, which can take both the advantages and the synergy of the PYT molecules and the graphene nanosheets.

Figure 4c,d shows the CV curves at different scan rates ( $2\text{--}50 \text{ mV s}^{-1}$ ) and the GCD curves under various current densities ( $0.5\text{--}5 \text{ A g}^{-1}$ ) of the optimized electrode (PYT/GN 4-5). With the increase of the scan rate, the oxidation and reduction peaks shift to more positive and more negative potentials, respectively, which can be attributed to the internal resistance.<sup>[59]</sup> Moreover, even at a scan rate of  $50 \text{ mV s}^{-1}$ , the shape of CV curves for the PYT/GN 4-5 electrode shows good preservation, indicating the high redox activity and good chemical reversibility of the PYT molecules within the composite electrode.<sup>[18]</sup> Moreover, the GCD curves (Figure 4d) of the PYT/GN 4-5 electrode display a nearly symmetrical shape at varying current densities, confirming the kinetic reversibility during the redox reaction in the PYT/GN 4-5 electrode.<sup>[60]</sup> The specific capacitance for all the electrodes can be calculated based on the GCD curves (Figure 4e). It is noted that, with the decrease of the mass ratio between the PYT and the GN from 8:1 to 4:5, the specific capacitance value increases monotonically. However, when the mass ratio is further reduced (PYT/GN 2-7), the specific capacitance decreases. The resulting PYT/GN 4-5 electrode with an optimized weight ratio, exhibits a higher specific capacity of 733, 711, 695, 686, 679, and  $673 \text{ F g}^{-1}$  at  $0.5\text{--}5 \text{ A g}^{-1}$ , respectively, which is considerably higher than that of the other electrodes. Besides, even at a current density of  $5 \text{ A g}^{-1}$ , the PYT/GN 4-5 electrode delivers a high specific capacity retention ratio of 91.5%, demonstrating its excellent rate performance. As shown in Figure S6, Supporting Information, the PYT/GN 4-5 electrode can retain 106.8% of the initial specific capacity after 5000 cycles at a current density of  $10 \text{ A g}^{-1}$ , indicating that the introduction of graphene can improve the stability of the hybrid electrode.

The charge storage mechanism of the PYT/GN 4-5 electrode can be further investigated via the relationship of scan rate ( $v$ ) and peak current ( $i$ ) as the following equation:  $i = av^b$  ( $\log(i/i) = b\log(v) + \log(a)$ ). The  $b$ -value can be determined from the slope of  $\log(i/i) - b\log(v)$  plots (Figure 4f). If  $b = 1$ , surface-controlled reaction dominates the energy storage process. If  $b = 0.5$ , the process is diffusion-controlled.<sup>[51]</sup> Herein, the  $b$ -values of the redox peaks are 0.90, 0.95, 0.95, and 0.86, which are very close to 1, indicating the surface-controlled reaction is the main charge storage process within the PYT/GN 4-5 electrode. Furthermore, the surface-controlled contribution of the total current at  $20 \text{ mV s}^{-1}$  is  $\approx 88.8\%$  (Figure S7, Supporting Information), further confirming that the pseudocapacitance dominates the charge storage process in the PYT/GN 4-5 hybrid electrode.

For comparison, the other type of reduced graphene oxide with a higher degree of reduction (LO),<sup>[61]</sup> was also introduced into the PYT-based composite electrodes to further explore how different source of graphene affects the electrochemical

performance of the composites. The electrochemical properties of the LO and the PYT/LO electrodes at different ratios are displayed in Figure 5. Notably, the CV area and the discharge time of the bare LO are relatively small (Figure 5a,b), implying a negligible capacity contribution. With the decrease of the mass ratio between the PYT and the LO from 8:1 to 2:7, the CV area and the discharge time of the composite electrodes are monotonously increasing, suggesting the enhancement of redox activity and the excellent energy storage capacity. As shown in Figure 5c, the shape of CV curves for the PYT/LO 2-7 electrode shows good preservation. The redox peaks of the PYT/LO 2-7 electrode are sharper than that of the PYT/GN 4-5 electrode, indicating the redox reaction of PYT molecules still dominates the charge storage process. The specific capacitances of all the electrodes (Figure 5e) can be calculated based on the GCD curves (Figure 5d and Figure S8, Supporting Information). The PYT/LO 2-7 electrode exhibits a specific capacity of 339, 331, 324, 320, 318, and  $316 \text{ F g}^{-1}$  at  $0.5\text{--}5 \text{ A g}^{-1}$ , respectively. In addition, the PYT/LO 2-7 electrode delivers excellent capacitance retention (around 98.5%) after 5000 cycles at a current density of  $10 \text{ A g}^{-1}$ , indicating the excellent stability of the hybrid electrode and further confirming the good interaction between the PYT and the LO (Figure S10, Supporting Information). Moreover, the  $b$ -values of the redox peaks are 0.82, 0.92, 0.82, and 0.89 (Figure 5f), which are close to 1, indicating the surface-controlled reaction is the main charge storage process within the PYT/LO 2-7 electrode.

Electrochemical impedance spectroscopy (EIS) of GN, LO, PYT/GN 4-5, PYT/GN 2-7, PYT/LO 4-5 and PYT/LO 2-7 is displayed in Figure S12a, Supporting Information with the corresponding equivalent circuit (Figure S12b, Supporting Information) to further understand the energy storage mechanism. Obviously, in the low-frequency region, all the electrodes show a nearly vertical line, indicating the low ionic ( $\text{H}^+$ ) diffusion impedance and good capacitive behavior.<sup>[62]</sup> In addition, the interception on the  $x$ -axis in the high-frequency region represents the ohmic resistance ( $R_s$ ), including the contact resistance between active materials and carbon paper substrate, the intrinsic resistance of active materials, and the ionic resistance of electrolyte.<sup>[60]</sup> As shown in the fitting results (Table S2, Supporting Information), the  $R_s$  values of the PYT-based composites are relatively larger than the pure graphene (LO and GN) due to the poor electrical conductivity of the PYT molecules. Furthermore, the diameter of the semicircle in the middle-frequency region corresponds to the charge-transfer resistance ( $R_{ct}$ ), reflecting the charge-transfer kinetics at the electrolyte-electrode interface.<sup>[63]</sup> Compared with the pure GN ( $0.96 \Omega$ ) and the pure LO ( $1.99 \Omega$ ) electrodes, the composite electrodes show smaller  $R_{ct}$  values, demonstrating a faster ion transfer process which may attribute to the improved wettability at the electrolyte-electrode interface.<sup>[64]</sup> The EIS results show that the constructed PYT-functionalized graphene electrodes display excellent electron/ion transport kinetics, which favors improving the electrochemical performance of the composite electrodes. Besides, compared with the PYT/LO-based electrodes, the PYT/GN composite electrodes possess much better electrochemical performance (Table S5, Supporting Information), due to the modest O content, the high surface area, and the synergy between the PYT molecules and the GN. Moreover, the as-obtained

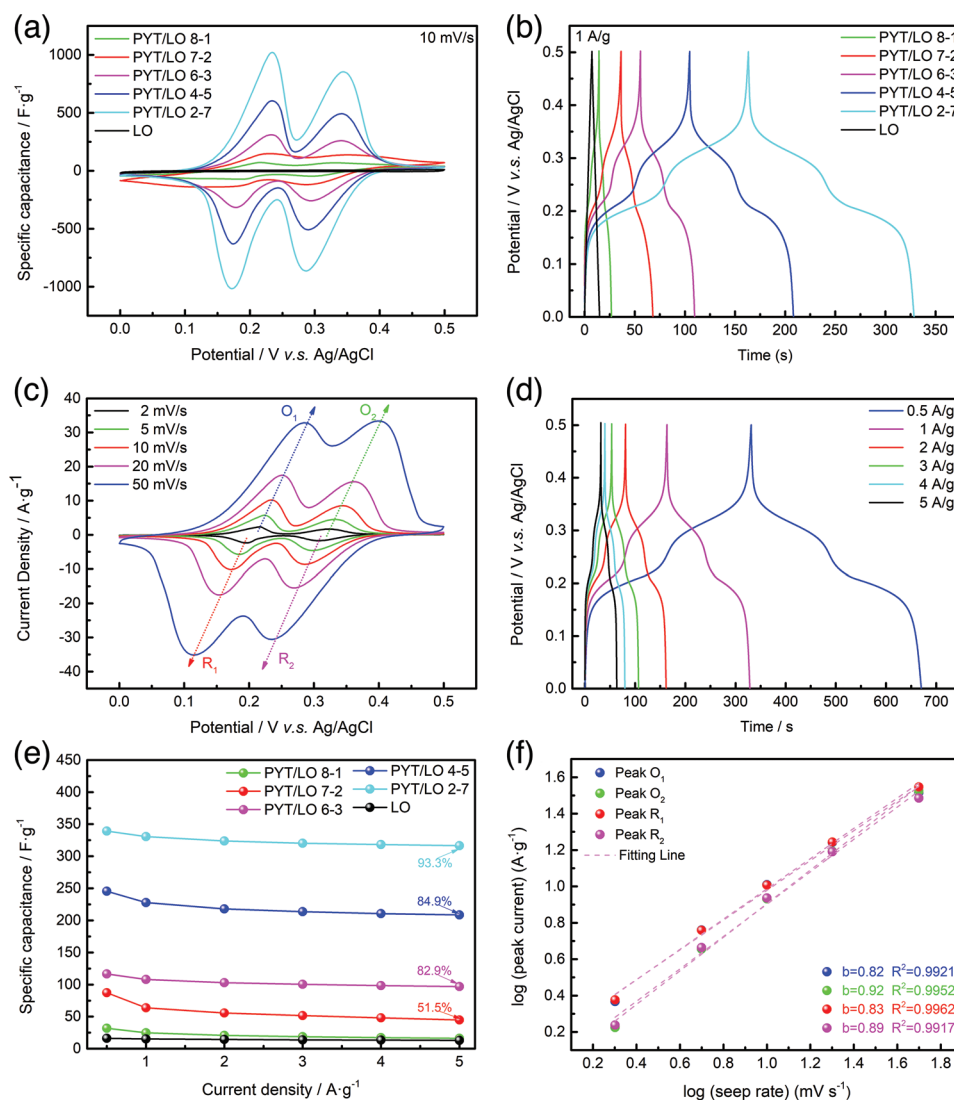


**Figure 5.** Electrochemical characterizations of different electrodes in a three-electrode system. a) CV curves at  $10 \text{ mV s}^{-1}$  and b) GCD curves at  $1 \text{ A g}^{-1}$ . c, d) CV curves at different scan rates and the corresponding GCD curves at various current densities of the PYT/LO 2–7 electrode. e) The specific capacity at various current densities and f) the relationship between peak current and scan rate.

PYT/GN 4–5 electrode offers tremendous competitiveness for energy storage compared with the previously reported organic molecule-based electrodes (Table S6, Supporting Information). The superior electrochemical performance of the PYT/GN 4–5 electrode results from the well-designed mass ratio between the PYT molecules and the GN, which can be attributed to the following reasons: 1) The introduction of GN can significantly improve the electronic conductivity of the composite electrodes and facilitate the redox reactivity of the PYT molecules; 2) The PYT molecules can effectively suppress the restacking and the aggregation of the graphene nanosheets, ensuring the rapid ion conduction and transport; 3) The reasonable component design of the PYT/GN 4–5 electrode can take both the advantages and the synergy between the PYT molecules and the GN; 4) The  $\pi$ – $\pi$  interactions between the redox-active PYT molecules and the GN, can improve the stability and rate performance of the hybrid electrode.<sup>[65]</sup>

### 2.3. Characterization and Electrochemical Performance of Anode

In order to match with the PYT/GN 4–5 cathode, the A- $\text{Ti}_3\text{C}_2\text{T}_x$  MXene was obtained after further calcination of the pure  $\text{Ti}_3\text{C}_2\text{T}_x$  MXene under an inert argon atmosphere. After etching, the  $\text{Ti}_3\text{C}_2\text{T}_x$  MXene shows a typical 2D sheet-like structure (Figures S13 and S14, Supporting Information), indicating the high exfoliation degree of  $\text{Ti}_3\text{C}_2\text{T}_x$ . After annealing, the A- $\text{Ti}_3\text{C}_2\text{T}_x$  MXene retains the shape of the nanosheets and the high electrical conductivity, which favors the charge transfer/transport kinetics.<sup>[66]</sup> The chemical compositions and the elemental valences on the surface of the  $\text{Ti}_3\text{C}_2\text{T}_x$  and the A- $\text{Ti}_3\text{C}_2\text{T}_x$  MXene were further investigated via XPS. Figure S15a, Supporting Information shows the wide-scan survey spectra, demonstrating the presence of C, O, F, and Ti elements, and the typical Al peak is not observed in the spectrum, confirming the complete etching of Al from the MAX phase. It is noted that the O content



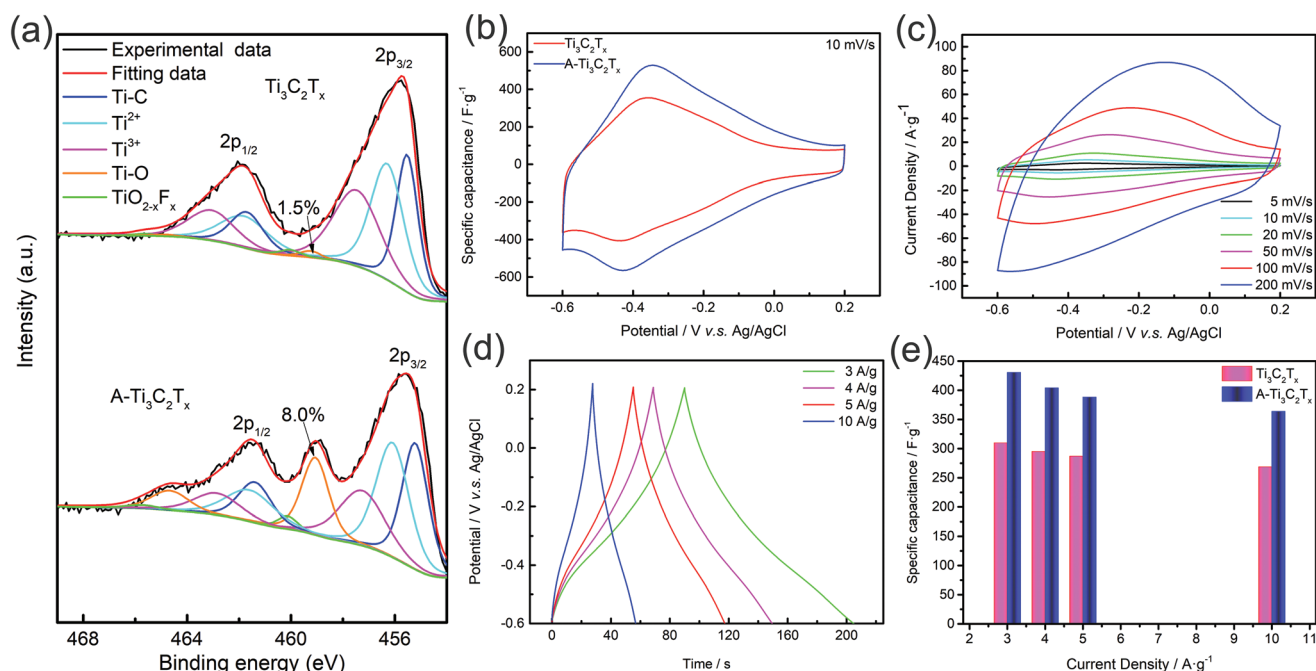


**Figure 6.** a) The high resolution of Ti2p spectra of the  $\text{Ti}_3\text{C}_2\text{T}_x$  and the  $\text{A-Ti}_3\text{C}_2\text{T}_x$ , b) comparison of the CV curves at  $10 \text{ mV s}^{-1}$ , c,d) CV curves at different scan rates and the corresponding GCD curves at various current densities of  $\text{A-Ti}_3\text{C}_2\text{T}_x$ , and e) comparison of the specific capacity at various current densities.

has an obvious increase from 18.1% to 30.0% and the F content decreases from 13.7% to 8.3% after the annealing treatment. Actually, surface F can occupy the electroactive sites and impede the transportation of ions, resulting in lower electrochemical performance.<sup>[67]</sup> As shown in the high-resolution O1s XPS spectra of the  $\text{Ti}_3\text{C}_2\text{T}_x$  and the  $\text{A-Ti}_3\text{C}_2\text{T}_x$  MXene (Figure S15b, Supporting Information), four peaks located at the binding energies of 530.2, 531.5, 532.5, and 533.6 eV can be assigned to the O–Ti( $\text{TiO}_2$ ), O–Ti(O/OH), O–C, and adsorbed water molecules ( $\text{H}_2\text{O}_{\text{ads}}$ ),<sup>[68,69]</sup> respectively. Meanwhile, the proportion of  $\text{H}_2\text{O}_{\text{ads}}$  decreased from 21.2% for the  $\text{Ti}_3\text{C}_2\text{T}_x$  to 10.5% for the  $\text{A-Ti}_3\text{C}_2\text{T}_x$  MXene, further confirming the removal of water on the surface of  $\text{Ti}_3\text{C}_2\text{T}_x$ . The F1s spectra (Figure S15c, Supporting Information) show two peaks at 685.4 and 686.7 eV, corresponding to the F–Ti and the F–C bonds, respectively. As shown in Figure 6a, the  $\text{Ti}2\text{p}_{3/2}$  spectrum can be fitted to five peaks at 455.5, 456.3, 457.5, 459.2, and 460.0 eV, attributed to the Ti–C,  $\text{Ti}^{2+}$ ,  $\text{Ti}^{3+}$ , Ti–O, and  $\text{TiO}_{2-x}\text{F}_x$ , respectively.<sup>[70]</sup> Apparently, the  $\text{Ti}2\text{p}$  spectrum of the  $\text{A-Ti}_3\text{C}_2\text{T}_x$  MXene shows a high percentage of the Ti–O bonds (8.0%), due to the change of the relative element content and the possible oxidation of the MXene during the annealing process. Moreover, the increased Ti/O ratio can provide more redox-active sites, resulting in an enhancement of the pseudocapacitive energy storage capability.<sup>[71]</sup>

The electrochemical properties of  $\text{Ti}_3\text{C}_2\text{T}_x$  and  $\text{A-Ti}_3\text{C}_2\text{T}_x$  MXene were studied using a three-electrode system in a 1 M  $\text{H}_2\text{SO}_4$  aqueous electrolyte. Compared with the pure  $\text{Ti}_3\text{C}_2\text{T}_x$  MXene, the  $\text{A-Ti}_3\text{C}_2\text{T}_x$  MXene electrode possesses a larger CV integral area (Figure 6b), suggesting its much higher specific capacitance after annealing. Even at a scan rate of  $200 \text{ mV s}^{-1}$ , the redox peaks of the CV curves for the  $\text{A-Ti}_3\text{C}_2\text{T}_x$  MXene (Figure 6c), remain a similar shape at various sweep speeds,

demonstrating the electrochemically reversible redox reactions and superior rate performance. In addition, all the CV curves show broad charge transfer peaks, which can be attributed to the pseudo-intercalation of  $\text{H}^+$  into the  $\text{A-Ti}_3\text{C}_2\text{T}_x$  MXene layers as the following reaction process.<sup>[26,72]</sup>

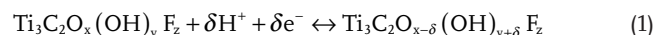
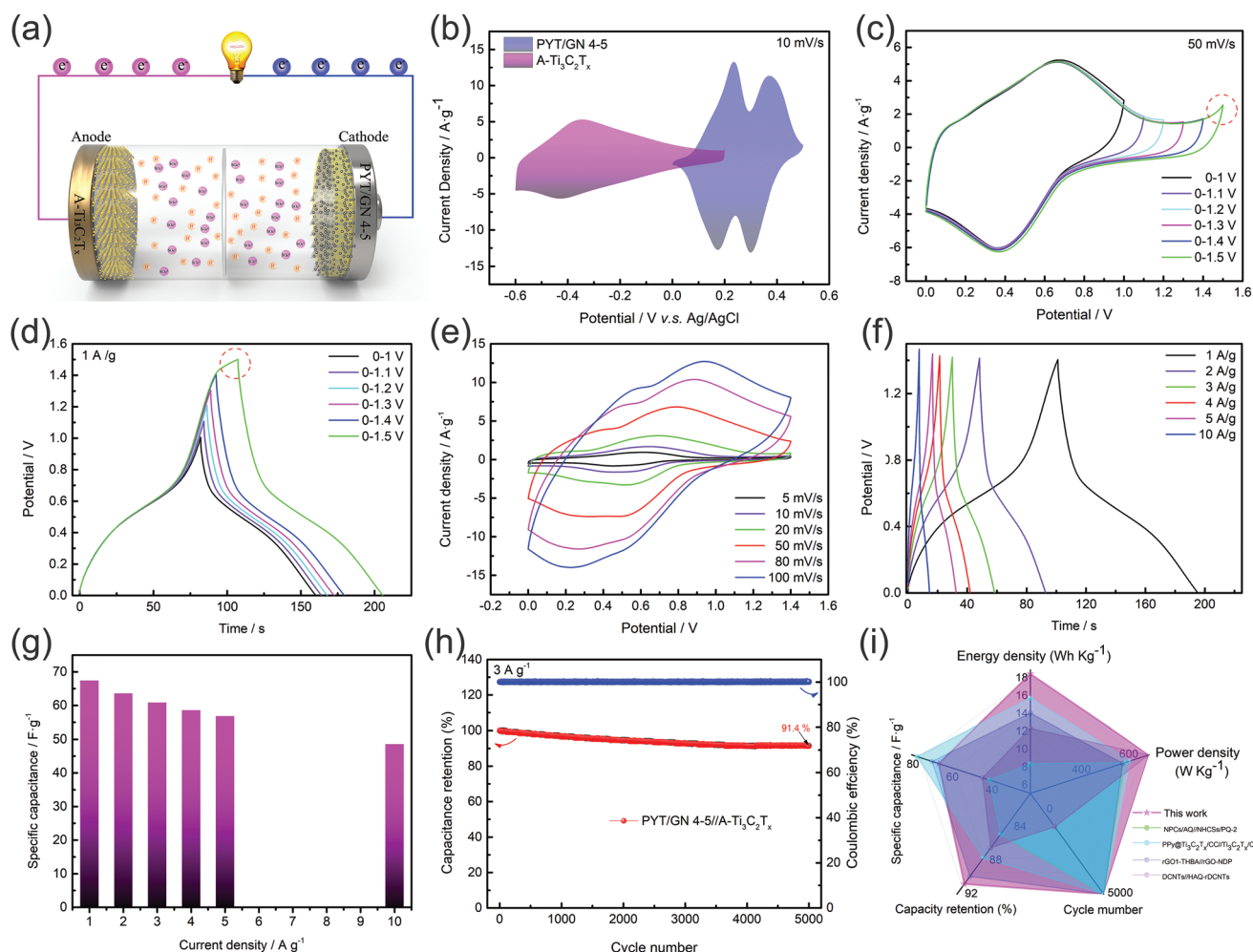


Figure 6d exhibits the GCD curves of the  $\text{A-Ti}_3\text{C}_2\text{T}_x$  MXene at varying current densities. Obviously, all the GCD curves show a nearly linear symmetrical triangle shape, indicating the typical pseudocapacitive character.<sup>[73]</sup> The specific capacitances of the  $\text{Ti}_3\text{C}_2\text{T}_x$  and the  $\text{A-Ti}_3\text{C}_2\text{T}_x$  MXene can be calculated based on the GCD curves and the results are shown in Figure 6e. The  $\text{A-Ti}_3\text{C}_2\text{T}_x$  MXene electrode exhibits a superior specific capacity of 431, 404, 388, and  $364 \text{ F g}^{-1}$  at 3–10  $\text{A g}^{-1}$ , which are higher than the specific capacities of the pure  $\text{Ti}_3\text{C}_2\text{T}_x$  MXene electrode (310, 295, 287, and  $269 \text{ F g}^{-1}$  at 3–10  $\text{A g}^{-1}$ , respectively). Therefore, the annealing process under proper conditions can be effective to enhance the electrochemical activity of the pure  $\text{Ti}_3\text{C}_2\text{T}_x$  MXene, due to the decrease of the F functional groups and the increase of the Ti–O content. In addition, as shown in Figure S17, Supporting Information, the  $\text{A-Ti}_3\text{C}_2\text{T}_x$  electrode exhibits a high capacitive contribution (82.4% of the total current at  $20 \text{ mV s}^{-1}$ ), further confirming that the charge storage mechanism is predominantly pseudocapacitive.

## 2.4. Asymmetric Supercapacitor Devices

The all-pseudocapacitive aqueous asymmetric supercapacitors (PYT/GN 4–5// $\text{A-Ti}_3\text{C}_2\text{T}_x$  ASCs), employing the PYT/GN





**Figure 7.** Electrochemical performance of the as-assembled PYT/GN 4-5//A-Ti<sub>3</sub>C<sub>2</sub>T<sub>x</sub> ASCs. a) Schematic illustration of the ASCs, b) CV curves of the PYT/GN 4-5 and the A-Ti<sub>3</sub>C<sub>2</sub>T<sub>x</sub> electrode at 10 mV s<sup>-1</sup> based on the three-electrode system, c,d) CV curves and GCD curves recorded at different potential windows, e) CV curves at different scan rates, f) GCD curves at various current densities, g) the specific capacitances, h) cycling life at 3 A g<sup>-1</sup>, and i) comparison of the electrochemical performance with other electrode materials in literature.

4-5 electrode as the cathode and the A-Ti<sub>3</sub>C<sub>2</sub>T<sub>x</sub> MXene as the anode, were assembled to further investigate its practical applications. The schematic illustration of the as-fabricated ASCs is displayed in Figure 7a, where the mass loading ratio of the PYT/GN 4-5 and the A-Ti<sub>3</sub>C<sub>2</sub>T<sub>x</sub> MXene is calculated to be approximately 1 based on the mentioned charge balance formula (the total active materials mass loading of the cathode and the anode is 3.2 mg). Figure 7b shows the CV curves of the PYT/GN 4-5 and the A-Ti<sub>3</sub>C<sub>2</sub>T<sub>x</sub> MXene at a scan rate of 10 mV s<sup>-1</sup>, and both of the electrodes exhibit a large capacitance at their respective potential windows. The CV and the GCD curves of the PYT/GN 4-5//A-Ti<sub>3</sub>C<sub>2</sub>T<sub>x</sub> ASC were recorded at different potential windows to ensure its feasibility and security. Evidently, the CV curves show a sharp peak once the operating voltage is over 1.4 V (Figure 7c), attributed to the evolution of oxygen.<sup>[74]</sup> Besides, the shape of the GCD curves changed at potential windows of 0–1.5 V (Figure 7d). Therefore, 0–1.4 V is an appropriate operating voltage for the PYT/GN 4-5//A-Ti<sub>3</sub>C<sub>2</sub>T<sub>x</sub> ASC. The CV curves of the PYT/GN 4-5//A-Ti<sub>3</sub>C<sub>2</sub>T<sub>x</sub> ASC show strong oxidation/reduction peaks (Figure 7e) due to the proton-coupled

electron exchange within the cathode and the anode.<sup>[75]</sup> Meanwhile, as the scan rate increases, the CV curves maintain a similar shape and the corresponding GCD curves (Figure 7f) exhibit a nearly symmetrical shape at different current densities, suggesting an excellent electrochemical stability as well as a fast charging/discharging process. Based on the total mass loading of the cathode and the anode, the PYT/GN 4-5//A-Ti<sub>3</sub>C<sub>2</sub>T<sub>x</sub> ASC exhibits a high specific capacitance (Figure 7g) of 674, 63.6, 60.9, 58.6, 56.8, and 48.6 F g<sup>-1</sup> at 1–10 A g<sup>-1</sup>, respectively. Furthermore, the as-assembled ASC delivers a capacitance retention of 91.4% and a high coulombic efficiency (over 99%) after 5000 cycles (Figure 7h), and even after 10 000 cycles, a capacitance retention of 83.8% can be obtained (Figure S19, Supporting Information), indicating good cycle stability.

As shown in Figure 7i, the PYT/GN 4-5//A-Ti<sub>3</sub>C<sub>2</sub>T<sub>x</sub> ASC exhibits an energy density as high as 18.4 Wh kg<sup>-1</sup> at a power density of 700 W kg<sup>-1</sup>. Even at the maximum power density of 7000 W kg<sup>-1</sup>, the energy density of 13.2 Wh kg<sup>-1</sup> can still be retained, which outperforms other reported organic electrode-based ASCs (Figure S20 and Table S7, Supporting

Information), such as the  $\text{Ti}_3\text{C}_2\text{T}_x/\text{PANI}@M\text{-Ti}_3\text{C}_2\text{T}_x$  ( $14.8 \text{ Wh kg}^{-1}$ ,  $700 \text{ W kg}^{-1}$ )<sup>[24]</sup> and  $\text{PPy}@Ti_3C_2T_x/CC//Ti_3C_2T_x/CC}$  ( $15.7 \text{ Wh kg}^{-1}$ ,  $620.8 \text{ W kg}^{-1}$ ).<sup>[76]</sup> Moreover, pseudocapacitive materials can undergo a faradaic process either on or near the surface of electrode materials. This process provides an opportunity to achieve excellent energy densities that are comparable to those of battery-type materials, while also offering a means of achieving high power density, similar to capacitive materials. In our work, the assembled PYT/GN 4–5//A- $\text{Ti}_3\text{C}_2\text{T}_x$  ASC (all-pseudocapacitive type materials) device provides inspiration for the design of energy storage devices with high energy and power density simultaneously.

### 3. Conclusion

In conclusion, the PYT served as a guest molecule to modify two kinds of graphene with different reduction degrees via a non-covalent strategy. PYT molecules can be functionalized onto the surface of the graphene sheets through noncovalent  $\pi$ - $\pi$  interactions, which favor preventing the stacking and the agglomeration of the graphene nanosheets. The resulting PYT-functionalized GN electrode (PYT/GN 4–5) demonstrates a high specific capacity of  $711 \text{ F g}^{-1}$  at  $1 \text{ A g}^{-1}$  and a good rate capability (91.5% of specific capacity retention ratio at  $5 \text{ A g}^{-1}$ ). In addition, to match with the PYT/GN 4–5 cathode, the A- $\text{Ti}_3\text{C}_2\text{T}_x$  was successfully prepared by annealing the pure  $\text{Ti}_3\text{C}_2\text{T}_x$  MXene under an inert argon atmosphere. Compared with the pure  $\text{Ti}_3\text{C}_2\text{T}_x$  MXene, the A- $\text{Ti}_3\text{C}_2\text{T}_x$  shows a better electrochemical performance due to the decrease of the F functional groups and the increase of the Ti–O content. The assembled PYT/GN 4–5//A- $\text{Ti}_3\text{C}_2\text{T}_x$  ASC delivers an outstanding energy density of  $18.4 \text{ Wh kg}^{-1}$  at a power density of  $700 \text{ W kg}^{-1}$ . The results confirm that the PYT-functionalized graphene holds great potential for next-generation energy storage devices. Our study represents an important step forward toward a deep understanding of the structure-property relationship, for the controlled fabrication of graphene-based multifunctional materials for ad-hoc applications including energy conversion and storage, nanocomposites, and membranes.

### 4. Experimental Section

**Materials and Reagents:**  $\text{Ti}_3\text{AlC}_2$  was purchased from Forsman (98%). Lithium fluoride (LiF, > 99%) and hydrochloric acid (HCl, ≥ 37%) were purchased from Sigma-Aldrich and the GN and LO graphene samples were purchased from Graphenea and LayerOne, respectively. All the chemicals were used directly without further treatment.

**Preparation of Pyrene-4,5,9,10-Tetraone:** The pyrene-4,5,9,10-tetraone (PYT) was prepared according to a previous report.<sup>[77]</sup>

**Preparation of  $\text{Ti}_3\text{C}_2\text{T}_x$  and A- $\text{Ti}_3\text{C}_2\text{T}_x$  MXene:** The etchant was prepared by adding 12 M LiF (320 mg) to 9 M HCl (4 mL). The solution mixture was stirred with a Teflon magnetic bar for 5 min in a polypropylene centrifuging tube. To this etchant, 200 mg of  $\text{Ti}_3\text{AlC}_2$  was slowly added and allowed to stir at  $50^\circ\text{C}$  for 24 h. Then the etched solution was washed repeatedly with water by centrifugation at 4000 rpm for 10 min. At a pH of ≈ 5–6, the delamination started. The dark green supernatant was obtained after centrifugation at 4000 rpm for 10 min. This process was repeated four times by adding water and shaking the whole solution by hand. All the solutions were combined, and the black solid

was obtained after centrifugation at 12 000 rpm for 30 min. Finally, the resulting solid was stored in degassed MilliQ water in a freezer. The as-obtained  $\text{Ti}_3\text{C}_2\text{T}_x$  MXene was annealed in a tube furnace at  $450^\circ\text{C}$  for 1 h with a heating rate of  $5^\circ\text{C min}^{-1}$  under an inert argon atmosphere, and the resulting sample was named as A- $\text{Ti}_3\text{C}_2\text{T}_x$  MXene.

**Structural Characterizations:** The morphology and microstructure of all the organic molecule electrodes were characterized by scanning electron microscopy (SEM, Quanta 200 FEG ESEM). The attenuated total reflectance infrared (ATR-IR) spectra were measured by a PerkinElmer frontier infrared spectrometer. UV–vis absorption spectra were recorded on a Varian Cary 50 Bio UV–vis spectrophotometer. The elemental composition and valence state of the samples were detected by the PHI 5000 VersaProbe III and the spectra were processed using the PHI MultiPak software. The electrical conductivity of as-obtained composites was measured by a four-probe resistivity meter (JANDEL RM3000).  $^1\text{H}$  NMR spectrum of the PYT molecule was recorded on a Varian NMR spectrometer (400 MHz).

**Electrochemical Measurements:** The as-obtained PYT molecules were mixed with different graphene (GN and LO) and 10 wt% of polyvinylidene fluoride (PVDF) in *N*-Methyl-2-pyrrolidone (NMP) to form a homogeneous slurry. The obtained slurry was uniformly pasted onto a conductive carbon paper and was further dried at  $60^\circ\text{C}$  under vacuum overnight. When GN was used as a conductive additive, the electrodes were named as PYT/GN  $x$ - $y$  ( $x/y = 8/1, 7/2, 6/3, 4/5, \text{ and } 2/7$ ), where  $x$  and  $y$  represented the mass ratio of PYT to GN. The mass loading of the PYT/GN  $x$ - $y$  was around  $1.7 \text{ mg cm}^{-2}$ . As a control, the electrode without the PYT molecules was denoted GN. For comparison, the electrodes, using LO as a conductive additive, were named as PYT/LO  $x$ - $y$  ( $x/y = 8/1, 7/2, 6/3, 4/5, \text{ and } 2/7$ ) and LO, respectively. For all the electrodes, the electrochemical measurement was performed on a Gamary electrochemical workstation (1010 E) using a three-electrode test system with a 1 M  $\text{H}_2\text{SO}_4$  aqueous solution as the electrolyte. Before starting the test, the electrolyte was purged with nitrogen. For the three-electrode system, active material-loaded carbon paper, Ag/AgCl in 3 M KCl, and a platinum net were employed as working, reference, and counter electrodes, respectively. The specific capacitance ( $C, \text{ F g}^{-1}$ ) of the individual electrode was calculated by the following formula.

$$C = I\Delta t / (m\Delta V) \quad (2)$$

where  $I$  (mA) is the current,  $\Delta t$  (s) is the discharge time,  $m$  (mg) is the mass loading of active materials on the carbon paper, and  $\Delta V$  (V) is the applied potential.

Two-electrodes system (PYT/GN 4–5//A- $\text{Ti}_3\text{C}_2\text{T}_x$  MXene ASCs) was assembled by employing the PYT/GN 4–5 electrode as the cathode and the A- $\text{Ti}_3\text{C}_2\text{T}_x$  MXene as the anode. Prior to the experiment, a three-electrode system was used to test the electrochemical properties of the  $\text{Ti}_3\text{C}_2\text{T}_x$  and the A- $\text{Ti}_3\text{C}_2\text{T}_x$  MXene in a 1 M  $\text{H}_2\text{SO}_4$  aqueous electrolyte purged with nitrogen, where the MXene-loaded carbon paper (about  $1 \text{ mg cm}^{-2}$ ), Ag/AgCl in 3 M KCl, and activated carbon (around  $6 \text{ mg cm}^{-2}$ ) were employed as working, reference, and counter electrodes, respectively. Moreover, the mass loading of the cathode and the anode can be balanced using the following formula.

$$Q^+ = Q^- \Rightarrow m^+ / m^- = C^- V^- / C^+ V^+ \quad (3)$$

The specific capacity of the PYT/GN 4–5//A- $\text{Ti}_3\text{C}_2\text{T}_x$  MXene ASCs could be calculated based on the total mass loading of the active materials (anode and cathode). The corresponding energy density ( $E, \text{ Wh kg}^{-1}$ ) and power density ( $P, \text{ W kg}^{-1}$ ) of the PYT/GN 4–5//A- $\text{Ti}_3\text{C}_2\text{T}_x$  MXene ASCs can be obtained.

$$E = 0.5C(\Delta V)^2 \quad (4)$$

$$P = E \times 3600 / \Delta t \quad (5)$$

Herein,  $\Delta V$  (V) and  $\Delta t$  (s) are the working potential and discharge time, respectively.

The detailed charge storage mechanism (the contribution of diffusion/surface-controlled kinetics) for the PYT/GN 4–5 and the A-Ti<sub>3</sub>C<sub>2</sub>T<sub>x</sub> MXene can be investigated via the following equation.

$$i_p = a\nu^b \quad (6)$$

Typically, the  $i_p$  is peak current,  $\nu$  is scan rates, and  $a$  and  $b$  are adjustable parameters. If  $b = 1$ , surface-controlled reaction dominates the energy storage process. If  $b = 0.5$ , the process is diffusion-controlled. Moreover, the diffusion/surface-controlled contribution can be further quantified using the following equation.

$$i(\nu) = k_1\nu + k_2\nu^{1/2} \quad (7)$$

where  $k_1\nu$  and  $k_2\nu^{1/2}$  represent the surface-/diffusion-controlled current, respectively. The above equation can be further converted to the following equation.

$$i(\nu)/\nu^{1/2} = k_1\nu^{1/2} + k_2 \quad (8)$$

The  $k_1$  and  $k_2$  values can be obtained from the slope of  $(i(\nu)/\nu^{1/2})$  and  $\nu^{1/2}$ .

## Supporting Information

Supporting Information is available from the Wiley Online Library or from the author.

## Acknowledgements

M.S. and P.C. contributed equally to this work. This work was financially supported by Stiftelsen Chalmers Tekniska Högskola, Adlerbertska Forskningsstiftelsen (C2020-1230, C2021-1258), Carl Tryggers Stiftelse (CTS 22:2286), Wenner-Gren Stiftelserna (2021-0183), Swedish Foundation for International Cooperation in Research and Higher Education (IB 2020–8789), Göteborg Energi (Tänk:Om Stipendiet), Swedish Research Council Starting Grant (2020-04903) and 2D TECH VINNOVA competence Center (Ref. 2019-00068). M.S. acknowledges the support from the China Scholarship Council (File No. 202106280242).

## Conflict of Interest

The authors declare no conflict of interest.

## Data Availability Statement

The data that support the findings of this study are available from the corresponding author upon reasonable request.

## Keywords

asymmetric supercapacitors, energy storage, graphene, MXene, redox-active organic molecules

Received: February 17, 2023  
Published online:

[1] A. Vlad, N. Singh, C. Galande, P. M. Ajayan, *Adv. Energy Mater.* **2015**, *5*, 1402115.

- [2] M. R. Lukatskaya, B. Dunn, Y. Gogotsi, *Nat. Commun.* **2016**, *7*, 1647.
- [3] P. Simon, Y. Gogotsi, *Nat. Mater.* **2020**, *19*, 1151.
- [4] C. Yang, D. Li, H. Gao, Q. Liu, J. Zhu, F. Wang, M. Jiang, *ACS Appl. Energy Mater.* **2020**, *3*, 2674.
- [5] D. Chao, W. Zhou, F. Xie, C. Ye, H. Li, M. Jaroniec, S. Qiao, *Sci. Adv.* **2020**, *6*, aba4098.
- [6] N. Díez, C. Botas, R. Mysyk, E. Goikolea, T. Rojo, D. Carriazo, *J. Mater. Chem. A* **2018**, *6*, 3667.
- [7] T. Guo, D. Zhou, L. Pang, S. Sun, T. Zhou, J. Su, *Small* **2022**, *18*, 2106360.
- [8] J. Li, L. An, H. Li, J. Sun, C. Shuck, X. Wang, Y. Shao, Y. Li, Q. Zhang, H. Wang, *Nano Energy* **2019**, *63*, 103848.
- [9] Z. Fan, J. Yan, T. Wei, L. Zhi, G. Ning, T. Li, F. Wei, *Adv. Funct. Mater.* **2011**, *21*, 2366.
- [10] K. S. Kumar, D. Pandey, J. Thomas, *ACS Energy Lett.* **2021**, *6*, 3590.
- [11] W. Zheng, J. Halim, Z. M. Sun, J. Rosen, M. W. Barsoum, *Energy Storage Mater.* **2021**, *38*, 438.
- [12] B. Huang, H. Wang, S. Liang, H. Qin, Y. Li, Z. Luo, C. Zhao, L. Xie, L. Chen, *Energy Storage Mater.* **2020**, *32*, 105.
- [13] K. Ren, Z. Liu, T. Wei, Z. Fan, *Nano-Micro Lett.* **2021**, *13*, 129.
- [14] G. Ma, F. Hua, K. Sun, E. Feng, Z. Zhang, H. Peng, Z. Lei, *Ionics* **2018**, *24*, 549.
- [15] L. Yang, K. Zhuo, X. Xu, Z. Zhang, Q. Du, G. Bai, J. Wang, *Electrochim. Acta* **2021**, *393*, 139057.
- [16] C. Zhou, T. Gao, Q. Liu, Y. Wang, D. Xiao, *Electrochim. Acta* **2020**, *336*, 135628.
- [17] Z. Zha, L. Xu, Z. Wang, X. Li, Q. Pan, P. Hu, S. Lei, *ACS Appl. Mater. Interfaces* **2015**, *7*, 17837.
- [18] R. Shi, C. Han, H. Duan, L. Xu, D. Zhou, H. Li, J. Li, F. Kang, B. Li, G. Wang, *Adv. Energy Mater.* **2018**, *8*, 1802088.
- [19] A. Ferris, S. Garbarino, D. Guay, D. Pech, *Adv. Mater.* **2015**, *27*, 6625.
- [20] J. Zhang, J. Jiang, H. Li, X. S. Zhao, *Energy Environ. Sci.* **2011**, *4*, 4009.
- [21] Y. Chen, C. Zhou, G. Liu, C. Kang, L. Ma, Q. Liu, *J. Mater. Chem. A* **2021**, *9*, 2872.
- [22] I. W. Ock, J. Lee, J. K. Kang, *Adv. Energy Mater.* **2020**, *10*, 2001851.
- [23] L. Qu, Y. Zhao, A. M. Khan, C. Han, K. M. Hercule, M. Yan, X. Liu, W. Chen, D. Wang, Z. Cai, W. Xu, K. Zhao, X. Zheng, L. Mai, *Nano Lett.* **2015**, *15*, 2037.
- [24] K. Li, X. Wang, S. Li, P. Urbankowski, J. Li, Y. Xu, Y. Gogotsi, *Small* **2020**, *16*, 1906851.
- [25] S. Ji, J. Yang, J. Cao, X. Zhao, M. A. Mohammed, P. He, R. A. W. Dryfe, I. A. Kinloch, *ACS Appl. Mater. Interfaces* **2020**, *12*, 13386.
- [26] Q. Sun, T. He, Y. Li, *J. Mater. Chem. A* **2020**, *8*, 1687.
- [27] Y. Xu, X. Chen, C. Huang, Y. Zhou, B. Fan, Y. Li, A. Hu, Q. Tang, K. Huang, *J. Power Sources* **2021**, *488*, 229426.
- [28] F. Ma, Z. Hu, L. Jiao, X. Wang, Y. He, Y. Yang, Z. Li, *ACS Appl. Energy Mater.* **2021**, *4*, 5493.
- [29] Z. Gan, J. Yin, X. Xu, Y. Cheng, T. Yu, *ACS Nano* **2022**, *16*, 5131.
- [30] C. Choi, D. S. Ashby, D. M. Butts, R. H. DeBlock, Q. Wei, J. Lau, B. Dunn, *Nat. Rev. Mater.* **2020**, *5*, 2058.
- [31] H. Yang, J. Lee, J. Y. Cheong, Y. Wang, G. Duan, H. Hou, S. Jiang, I. D. Kim, *Energy Environ. Sci.* **2021**, *14*, 4228.
- [32] J. Shi, Z. Zhao, J. Wu, Y. Yu, Z. Peng, B. Li, Y. Liu, H. Kang, Z. Liu, *ACS Sustainable Chem. Eng.* **2018**, *6*, 4729.
- [33] H. Zhou, A. Uysal, D. M. Anjos, Y. Cai, S. H. Overbury, M. Neurock, J. K. McDonough, Y. Gogotsi, P. Fenter, *Adv. Mater. Interfaces* **2015**, *2*, 1500277.
- [34] C. Peng, X. Zhang, *Chemistry* **2021**, *3*, 873.
- [35] Y. Zhao, J. Liu, N. Wang, Q. Li, M. Hu, *J. Mater. Chem. A* **2018**, *6*, 7566.
- [36] L. Wang, Z. Liu, J. Zhang, *Nanoscale* **2022**, *14*, 13473.
- [37] A. C. Ferrari, F. Bonaccorso, V. Fal'ko, K. S. Novoselov, S. Roche, P. Bøggild, S. Borini, F. H. L. Koppens, V. Palermo, N. Pugno, J. A. Garrido, R. Sordan, A. Bianco, L. Ballerini, M. Prato, E. Lidorikis,

- J. Kivioja, C. Marinelli, T. Ryhänen, A. Morpurgo, J. N. Coleman, V. Nicolosi, L. Colombo, A. Fert, M. Garcia-Hernandez, A. Bachtold, G. F. Schneider, F. Guinea, C. Dekker, M. Barbone, et al., *Nanoscale* **2015**, 7, 4598.
- [38] M. Pumera, *Energy Environ. Sci.* **2011**, 4, 668.
- [39] J. Zhu, D. Yang, Z. Yin, Q. Yan, H. Zhang, *Small* **2014**, 10, 3480.
- [40] C. Backes, A. M. Abdelkader, C. Alonso, A. Andrieux-Ledier, R. Arenal, J. Azpeitia, N. Balakrishnan, L. Banszerus, J. Barjon, R. Bartali, S. Bellani, C. Berger, R. Berger, M. M. B. Ortega, C. Bernard, P. H. Beton, A. Beyer, A. Bianco, P. Bøggild, F. Bonaccorso, G. B. Barin, C. Botas, R. A. Bueno, D. Carriazo, A. Castellanos-Gomez, M. Christian, A. Ciesielski, T. Ciuk, M. T. Cole, J. Coleman, et al., *2D Mater.* **2020**, 7, 022001.
- [41] Z. S. Wu, G. Zhou, L. C. Yin, W. Ren, F. Li, H. M. Cheng, *Nano Energy* **2012**, 1, 107.
- [42] L. Xu, R. Shi, H. Li, C. Han, M. Wu, C. P. Wong, F. Kang, B. Li, *Carbon* **2018**, 127, 459.
- [43] H. Cui, P. Hu, Y. Zhang, W. Huang, A. Li, *ChemElectroChem* **2021**, 8, 352.
- [44] Y. Wen, T. E. Rufford, X. Chen, N. Li, M. Lyu, L. Dai, L. Wang, *Nano Energy* **2017**, 38, 368.
- [45] J. Zhang, S. Seyedin, S. Qin, Z. Wang, S. Moradi, F. Yang, P. A. Lynch, W. Yang, J. Liu, X. Wang, J. M. Razal, *Small* **2019**, 15, 1804732.
- [46] D. Xiong, X. Li, Z. Bai, S. Lu, *Small* **2018**, 14, 1703419.
- [47] Q. Zhu, J. Li, P. Simon, B. Xu, *Energy Storage Mater.* **2021**, 35, 630.
- [48] M. Boota, M. Rajesh, M. Bécuwe, *Mater. Today Energy* **2020**, 18, 100532.
- [49] S. Liu, F. Hu, W. Shao, W. Zhang, T. Zhang, C. Song, M. Yao, H. Huang, X. Jian, *Nano-Micro Lett.* **2020**, 12, 135.
- [50] J. Come, Y. Xie, M. Naguib, S. Jesse, S. V. Kalinin, Y. Gogotsi, P. R. C. Kent, N. Balke, *Adv. Energy Mater.* **2016**, 6, 1502290.
- [51] L. Jiao, F. Ma, X. Wang, Z. Li, Z. Hu, Q. Yin, *ACS Appl. Energy Mater.* **2021**, 4, 7811.
- [52] B. Yang, Y. Ma, D. Bin, H. Lu, Y. Xia, *ACS Appl. Mater. Interfaces* **2021**, 13, 58818.
- [53] C. Guo, Y. Liu, L. Wang, D. Kong, J. Wang, *ACS Sustainable Chem. Eng.* **2022**, 10, 213.
- [54] L. Lv, Z. Hu, N. An, K. Xie, Y. Yang, Z. Zhang, Z. Li, *Electrochim. Acta* **2021**, 377, 138088.
- [55] R. Al-Gaashani, A. Najjar, Y. Zakaria, S. Mansour, M. A. Atieh, *Ceram. Int.* **2019**, 45, 14439.
- [56] Y. Ma, Z. Guo, X. Dong, Y. Wang, Y. Xia, *Angew. Chem., Int. Ed.* **2019**, 58, 4622.
- [57] M. Li, J. Liu, Y. Li, G. Xing, X. Yu, C. Peng, L. Chen, *CCS Chem.* **2021**, 3, 696.
- [58] Y. Gogotsi, R. M. Penner, *ACS Nano* **2018**, 12, 2081.
- [59] X. Yang, Y. Yang, Q. Zhang, X. Wang, Y. An, B. Guo, Z. Hu, H. Wu, *RSC Adv.* **2017**, 7, 48341.
- [60] L. Xu, Y. Zhang, W. Zhou, F. Jiang, H. Zhang, Q. Jiang, Y. Jia, R. Wang, A. Liang, J. Xu, X. Duan, *ACS Appl. Mater. Interfaces* **2020**, 12, 45202.
- [61] M. Pelaez-Fernandez, A. Bermejo, A. M. Benito, W. K. Maser, R. Arenal, *Carbon* **2021**, 178, 477.
- [62] W. Zhang, L. Chen, H. Liu, H. Kang, S. Zhang, B. Yang, Y. Wang, M. Yuan, Z. Li, *Electrochim. Acta* **2020**, 332, 135528.
- [63] M. Yao, C. Guo, Q. Geng, Y. Zhang, X. Zhao, X. Zhao, Y. Wang, *Ind. Eng. Chem. Res.* **2022**, 66, 7480.
- [64] L. Wang, X. Ye, Y. Zhu, H. Jiang, J. Xia, Z. Yue, Z. Wan, C. Jia, X. Yao, *Electrochim. Acta* **2020**, 340, 135804.
- [65] M. Boota, M. Bécuwe, Y. Gogotsi, *ACS Appl. Energy Mater.* **2020**, 3, 3144.
- [66] W. Liu, Y. Zheng, Z. Zhang, Y. Zhang, Y. Wu, H. Gao, J. Su, Y. Gao, *J. Power Sources* **2022**, 521, 230965.
- [67] J. Chen, M. Chen, W. Zhou, X. Xu, B. Liu, W. Zhang, C. Wong, *ACS Nano* **2022**, 16, 2461.
- [68] Y. Liu, Y. Tian, Q. Han, J. Yin, J. Zhang, Y. Yu, W. Yang, Y. Deng, *Chem. Eng. J.* **2021**, 410, 128209.
- [69] S. Thurakkal, X. Zhang, *Mater. Chem. Front.* **2022**, 6, 561.
- [70] J. Halim, K. M. Cook, M. Naguib, P. Eklund, Y. Gogotsi, J. Rosen, M. W. Barsoum, *Appl. Surf. Sci.* **2016**, 362, 406.
- [71] M. Yao, Y. Chen, Z. Wang, C. Shao, J. Dong, Q. Zhang, L. Zhang, X. Zhao, *Chem. Eng. J.* **2020**, 395, 124057.
- [72] X. Mu, D. Wang, F. Du, G. Chen, C. Wang, Y. Wei, Y. Gogotsi, Y. Gao, Y. Dall'Agnese, *Adv. Funct. Mater.* **2019**, 29, 1902953.
- [73] S. Fleischmann, J. B. Mitchell, R. Wang, C. Zhan, D. Jiang, V. Presser, V. Augustyn, *Chem. Rev.* **2020**, 120, 6738.
- [74] J. Zhou, Q. Kang, S. Xu, X. Li, C. Liu, L. Ni, N. Chen, C. Lu, X. Wang, L. Peng, X. Guo, W. Ding, W. Hou, *Nano Res.* **2022**, 15, 285.
- [75] F. Ma, Z. Hu, L. Jiao, X. Wang, Y. Yang, Z. Li, Y. He, *Adv. Mater. Interfaces* **2021**, 8, 2002161.
- [76] X. Chen, F. Su, Q. Zhou, J. Sun, *Surf. Interfaces* **2021**, 26, 101393.
- [77] J. Hu, D. Zhang, F. W. Harris, *J. Org. Chem.* **2005**, 70, 707.